Monthly Notices of the ROYAL ASTRONOMICAL SOCIETY

MNRAS **498,** 926–939 (2020)
Advance Access publication 2020 July 9

doi:10.1093/mnras/staa1989

Simulating kilonovae in the ΛCDM universe

Zhen Jiang,[1,2]★ Jie Wang,[1,2]★ Fenghui Zhang,[3,4] Li-Xin Li,[5] Lan Wang,[1] Ran Li,[1,2] Liang Gao,[1,2,6] Zhanwen Han[3,4,7] and Jun Pan[1]

[1]*Key Laboratory for Computational Astrophysics, National Astronomical Observatories, Chinese Academy of Sciences, Beijing 100012, China*
[2]*School of Astronomy and Space Science, University of Chinese Academy of Sciences, Beijing 100049, China*
[3]*Yunnan Observatories, Chinese Academy of Sciences, Kunming 650216, China*
[4]*Key Laboratory for the Structure and Evolution of Celestial Objects, Chinese Academy of Sciences, Kunming 650216, China*
[5]*Kavli Institute for Astronomy and Astrophysics, Peking University, Beijing 100871, China*
[6]*Institute of Computational Cosmology, Department of Physics, University of Durham, South Road, Durham DH1 3LE, UK*
[7]*Center for Astronomical Mega-Science, Chinese Academy of Sciences, 20A Datun Road, Chaoyang District, Beijing 100012, China*

Accepted 2020 July 3. Received 2020 July 3; in original form 2020 January 28

ABSTRACT

Kilonovae are optical flashes produced in the aftermath of neutron star–neutron star mergers or neutron star–black hole mergers. In this work, we use the Millennium Simulation, combined with semi-analytic galaxy formation model GABE (Galaxy Assembly with Binary Evolution) to explore the cosmic event rate of kilonovae, and the properties of their host galaxies in a cosmological context. We find that model with supernova kick velocity of $V_{\rm kick} = 0$ km s^{-1} fits the observation best, satisfying the preference for low kick velocity binary system in theoretical models. With $V_{\rm kick} = 0$ km s^{-1}, the cosmic event rate of NNMs and NBMs at $z = 0$ are 283 and 91 Gpc^{-3} yr^{-1}, respectively, marginally consistent with the constraint from LVC GWTC-1. For Milky Way-mass galaxies, we predict the NNM rate is $25.7^{+59.6}_{-7.1}$ Myr^{-1}, which is also in good agreement with the observed properties of binary neutron stars in the Milky Way. Taking all the kilonovae into account in the history of Milky Way-mass galaxies, we find that the averaged r-process elements yield ($A > 79$) in an NNM/NBM event should be 0.01 M$_\odot$ to be consistent with observation. We conclude that NGC 4993, the host galaxy of GW170817, is a typical host galaxy for NNMs. However, generally, NNMs and NBMs tend to reside in young, blue, star-forming, late-type galaxies, with stellar mass, and gaseous metallicity distribution peaking at $M_* = 10^{10.65}$ M$_\odot$ and $12 + \log({\rm O/H}) = 8.72 - 8.85$, respectively. By exploring the connection between kilonovae and their host galaxies in the cosmological background, it is promising to constrain model better when we have more events in the forthcoming future.

Key words: nuclear reactions, nucleosynthesis, abundances – binaries: general – supernovae: general – galaxies: general – black hole - neutron star mergers – neutron star mergers.

1 INTRODUCTION

When a neutron star–neutron star merger (NNM) happens, neutron-rich material is ejected subrelativistically and a black hole or a neutron star is left over as a remnant (Abbott et al. 2017d; Yu, Liu & Dai 2018). The neutron-rich expanding ejecta provides an excellent nursery for rapid neutron capture (r-process) nucleosynthesis. The decay radiation of these newly formed r-process elements is the so-called kilonova (Li & Paczyński 1998; Metzger et al. 2010; Metzger 2017), which is expected to appear days after merger and peak at ultraviolet (UV), optical, or near-infrared wavelengths, depending on the opacity of ejecta (Li & Paczyński 1998; Barnes & Kasen 2013; Kasen, Badnell & Barnes 2013; Tanaka & Hotokezaka 2013). Kilonova was first directly observed through infrared emission excess about one week after SGRB 130603B (Berger, Fong & Chornock 2013; Tanvir et al. 2013). Note that theoretically, neutron star–black hole mergers (NBMs) can also eject neutron-rich matter with subrelativistic velocity and trigger kilonovae (e.g. Lattimer & Schramm 1974; Surman et al. 2008).

On 2017 August 17, the first directly detected NNM, GW170817, was observed by Advanced LIGO detectors (LIGO Scientific Collaboration et al. 2015; Abbott et al. 2017a). This was the only NNM event observed in the first (O1) and second (O2) observing run of Advanced LIGO (O1 spanned four months and O2 spanned nine months). Other detection was all black hole–black hole mergers (BBMs), with 10 confidently identified detection (Abbott et al. 2019b). No NBMs were detected. Considering all available data from O1 and O2, LIGO Scientific Collaboration and Virgo Collaboration (LVC) infer that the cosmic event rate of NNMs is 1210^{+3230}_{-1040} Gpc^{-3} yr^{-1} with 90 per cent confidence, and the 90 per cent upper limit of the cosmic event rate of NBMs is 610 Gpc^{-3} yr^{-1} (Abbott et al. 2019a).

GW170817 had a high combined signal-to-noise ratio of 32.4, which allowing its sky localization narrowed to 28 deg^2 at 90 per cent probability. In this sky region, the electromagnetic (EM) counterparts of GW170817 in γ-ray, X-ray, UV, optical, infrared, and radio bands were recognized by EM follow-up campaign (summarized in Abbott et al. 2017b). Its EM emission peaked < 1 day in UV,

★ E-mail: zjiang@nao.cas.cn (ZJ); jie.wang@nao.cas.cn (JW)

indicating a blue component with low opacity, and then slowly shifted towards near-infrared days after merger, which can be fitted with a two-component kilonova model (Cowperthwaite et al. 2017; Nicholl et al. 2017; Tanvir et al. 2017; Waxman et al. 2018; Li 2019). NGC 4993 was confirmed to be the host galaxy, as the EM counterpart of GW170817 was near NGC 4993 and NGC 4993 shares the consistent distance inferred from gravitational wave (GW) data (Coulter et al. 2017). NGC 4993 is an old elliptical galaxy with stellar mass of $\log(M_*/\mathrm{M}_\odot) = 10.65^{+0.03}_{-0.03}$ and median mass-weighted age of $13.2^{+0.5}_{-0.9}$ Gyr as measured by Blanchard et al. (2017). Troja et al. (2017) reported a similar stellar mass, $\log(M_*/\mathrm{M}_\odot) = 10.7-11.0$, but with a younger age of 3−7 Gyr. As the spectra of long-lived stars evolve quite slowly, the age estimation of stellar populations of old galaxies has large systematic errors.

The third (O3) observing run of LVC[1] began on 2019 April 1 and is planned to end on 2020 April 30. Till the end of 2019, with nine months' observation, three NNMs, and two NBMs (probability > 99 per cent) have been detected. Among them, S190425z (LIGO Scientific Collaboration & VIRGO Collaboration 2019) has a probability > 99 per cent to be an NNM, with a false alarm rate (FAR) of 1 per 69 834 yr. A weak γ-ray burst which consisted of two pulses (∼0.5 and ∼5.9 s later separately) was detected by *INTEGRAL*, in the northern region of the localization proposed by LVC (Pozanenko et al. 2020). However, following observations have not yet confirmed any optical counterpart of S190425z (Coughlin et al. 2019; Hosseinzadeh et al. 2019; Lundquist et al. 2019; Antier et al. 2020). S190814bv[2] has a probability > 99 per cent to be an NBM, with an extremely low FAR of 1 per 1.559×10^{25} yr. Unfortunately, no EM counterparts were confirmed in the following observing campaign till the end of 2019 (Andreoni et al. 2019; Dobie et al. 2019; Gomez et al. 2019). Information about candidates and host galaxies of other events are not public yet. As O3 is still going on and its updates on NNMs and NBMs event rate and host galaxies have not been published, we stick to the observational result of LVC O1 and O2 (LVC GWTC-1, Abbott et al. 2019a) as the comparison with our model prediction in this work.

From the modelling point of view, the traditional way to estimate the NNM event rate in a galaxy is to convolve the NNM event rates of simple stellar populations (SSPs), which are derived from stellar population synthesis models with a hypothetical star formation history. For instance, based on observational results (e.g. Gilmore 2001), a constant star formation rate of $3.5-4.0\,\mathrm{M}_\odot\,\mathrm{yr}^{-1}$ that lasts for 10−12 Gyr is usually assumed to estimate the NNM event rate in the Milky Way (Portegies Zwart & Yungelson 1998; Belczynski, Kalogera & Bulik 2002; Voss & Tauris 2003; Belczynski et al. 2007; Dominik et al. 2012; Belczynski et al. 2016; Chruslinska et al. 2018; Belczynski et al. 2018a,b). With the estimated event rate in the Milky Way, Belczynski et al. (2007, 2016) simply extended the results to other galaxies and estimated a rough number on the cosmic event rate. Therefore, the uncertainties and systematic errors hide in this simple approach is expected not small. Except for the hypothetical star formation histories, fitting formulas of the observed cosmic star formation density history (Strolger et al. 2004; Madau & Dickinson 2014) can also be used to estimate the cosmic event rate density (Dominik et al. 2013; Chruslinska et al. 2018; Boco et al. 2019). In recent years, due to the fast development of cosmological hydrodynamic simulations, star formation histories from cosmological hydrodynamic simulations are more frequently used to estimate NNM event rate (Mapelli & Giacobbo 2018; Mapelli et al. 2018, 2019; Toffano et al. 2019; Artale et al. 2019, 2020). Star formation histories of various galaxies derived from semi-empirical models (Behroozi et al. 2019) are also used (Adhikari et al. 2020).

In this work, we use semi-analytic models of galaxy formation to estimate the cosmic event rate of kilonova events, triggered by both NNMs and NBMs (hereafter denoted as compact object mergers, COMs), and study the properties of their host galaxies. Combined with N-body merger trees of dark matter haloes, semi-analytic models trace how galaxies form and evolve in haloes, by implementing simplified models or empirical relations that describe physical processes including reionization, gas cooling, star formation, supernova feedback, black hole growth, AGN feedback, galaxy mergers, etc., and have recovered a large amount of observations in the local Universe and at high redshift (e.g. White & Frenk 1991; Kauffmann et al. 1999; Croton et al. 2006; De Lucia & Blaizot 2007; Guo et al. 2011; Henriques et al. 2015). With semi-analytic models, the star formation histories of galaxies in a large mass range, from dwarf satellite galaxies to BCGs (the Brightest Cluster Galaxy), are specified from the first principle, which allows us to derive NNM and NBM event rates for each galaxy, and to explore the relationship between kilonovae and their host galaxies. Besides, semi-analytic models consume much less computational time than cosmological hydrodynamic simulations, which allows us to generate galaxy catalogue for a larger volume.

The semi-analytic model, we use in this study is GABE (Galaxy Assembly with Binary Evolution; Jiang et al. 2019), which includes a full set of galaxy formation recipes and has reproduced a large body of observational results. Compared with previous semi-analytic models, GABE for the first time modelled binary star evolution by adopting YUNNAN-II stellar population synthesis model, which includes various interactions of binaries. Therefore, it is able to use GABE to make direct predictions of binary population in the simulated galaxies. In particular, the remnants of binary stars, i.e. all kinds of double compact objects, including double neutron stars (NS–NS), neutron star-black hole (NS–BH) and double black holes (BH–BH), can be modelled and predicted in detail.

The structure of this paper is as follows. In Section 2, we first introduce briefly the semi-analytic model GABE and YUNNAN-II stellar population synthesis model we use, then describe our method to calculate NNM and NBM event rates in SSP and in galaxies. In Sections 3.1 and 3.2, we show the event rates of NNMs and NBMs for both SSP and for modelled galaxies in a cosmological point of view. Section 3.3 shows the prediction of r-process elements produced by COMs in the lifetimes of galaxies. In Section 4, properties of COM host galaxies are presented. We summarize our conclusions in Section 5.

2 MODELS AND METHODS

2.1 Semi-analytic model

The semi-analytic galaxy formation model used in this work is GABE (Jiang et al. 2019), which includes detailed modelling of BSE by adopting YUNNAN-II stellar population synthesis model (introduced later in Section 2.2). More details about the model can be found in Jiang et al. (2019).

The Millennium Simulation (Springel et al. 2005) is used to implement GABE in this work. The cosmological parameters adopted are: Ω_m(matter density) = 0.25, Ω_b(baryon density) = 0.045, Ω_Λ(dark energy density) = 0.75, n(spectral index) = 1, σ_8 (linear predictions for the amplitude of fluctuations within $8\,h^{-1}$ Mpc) = 0.9 and

[1] https://gracedb.ligo.org/superevents/public/O3/
[2] https://gracedb.ligo.org/superevents/S190814bv/view/

H_0(Hubble constant) = 73 km s^{-1} Mpc^{-1}, derived from a combined analysis of the 2dFGRS (Colless et al. 2001) and the first-year WMAP data (Spergel et al. 2003). Though these cosmological parameters were outdated since the release of Planck Collaboration XIII (2015), as shown by Wang et al. (2008), Fontanot et al. (2012), Guo et al. (2013) and Henriques et al. (2015), changing cosmological parameters between WMAP series and *PLANCK* cosmology has much smaller influence on galaxy properties than the uncertainties in galaxy formation models. Thus switching to the newest *PLANCK* cosmology has little impact on our conclusions. Dark matter haloes and subhaloes in the simulation are identified with a friends-of-friends group finder (Davis et al. 1985) and SUBFIND (Springel et al. 2001), respectively. The merger trees are derived by following the formation and merger history of each halo/subhalo with the D-Tree algorithm (Jiang et al. 2014), based on which GABE is applied to.

The simulation's box size is 685 Mpc, which is large enough to suppress cosmic variance so that we can conduct reliable statistics (Wang et al. 2017). Besides, it is also large enough to be compared with the detectable horizon of current ground-based GW detectors, ranging from 58 to 218 Mpc for NNMs (Abbott et al. 2017a). The mass resolution of dark matter particle in the Millennium Simulation is 1.2 × 10^9 $M_\odot$, allowing GABE to generate a complete galaxy catalogue for galaxies more massive than $\sim 10^9 M_\odot$. This galaxy sample is enough for us to study the cosmic statistic properties of NNM/NBMs and their host galaxies with typical characteristic stellar mass.

2.2 Stellar population synthesis models

YUNNAN-II stellar population synthesis model (Zhang et al. 2004, 2005, 2010) is used to model binary evolution in GABE. YUNNAN-II is a stellar population synthesis model developed by the Group of Binary Population Synthesis of Yunnan Observatories. It is built based on the rapid binary star evolution (BSE) algorithm of Hurley, Tout & Pols (2002), which modelled various binary interactions including mass transfer, mass accretion, common-envelope evolution, collisions, supernova kicks, tidal evolution and angular momentum loss through GWs. In Zhang et al. (2010), the evolutionary population synthesis models of Han, Podsiadlowski & Lynas-Gray (2007), which considered sub-dwarf B stars (sdBs) were also included. By combining the binary evolution of YUNNAN-II model with the star formation histories of GABE, instead of only modelling single-star evolution as in Bruzual & Charlot (2003), properties of binary stars in galaxies can be studied.

The setting of initial parameters of YUNNAN-II model and updated model parameters can be found in section 2.4.1 of Jiang et al. 2019. Here, we briefly describe the changes we have made in this work based on the fiducial YUNNAN-II model. (1) The range of the initial mass of the primary star in a binary is changed from [0.1, 100] to [5, 100] $M_\odot$, to focus on binaries that can have remnants of neutron stars and black holes that we are studying. (2) The initial mass function (IMF) of Chabrier 2003 is used, replacing the approximated IMF given by Eggleton, Fitchett & Tout 1989. (3) The maximum mass of neutron star is set to be 3.0 $M_\odot$, rather than 1.8 $M_\odot$ in the oiriginal BSE. (4) The dispersion of the kick velocities of supernovae,[3] which are the natal velocities of the remnants after supernovae due to the asymmetry of explosion, are set to be able to vary in the range from 0 to 190 km s^{-1}, instead of the fixed value of 190 km s^{-1} in the fiducial YUNNAN-II model. As we find that the value of kick velocity influence the merger rate a lot (∼2 mag, see Fig. 1). Large kick velocities will enlarge the orbital separations after supernova and delay the coalescence. Binary systems could even be tore apart with larger kick velocities. Thus, increasing kick velocities will lower the merger rate. Besides, there are studies indicate that kick velocities in binary systems could be lower than ones of single stars in some cases (Podsiadlowski et al. 2004; Dewi, Podsiadlowski & Pols 2005; Tauris, Langer & Podsiadlowski 2015; Tauris et al. 2017, see Section 3.2 for more details). Four values of $V_{\rm kick}$ = 0, 50, 100, 190 km s^{-1} are applied and checked in Sections 3.1 and 3.2. From Section 3.3, $V_{\rm kick}$ = 0 km s^{-1} is chosen to build our fiducial model, since with this value the predicted cosmic event rate density is more consistent with the observational constraint of LVC in the local Universe, as can be seen in Fig. 3 and Section 3.2.

Note that apart from the kick velocity of supernovae, other model parameters of stellar population synthesis model, such as common-envelope parameter and mass-transfer parameter, could also affect the merger rate (e.g. Dominik et al. 2012; Chruslinska et al. 2018). While the focus of this work is the evolution of COMs and their host galaxies. A full exploration of the parameter space

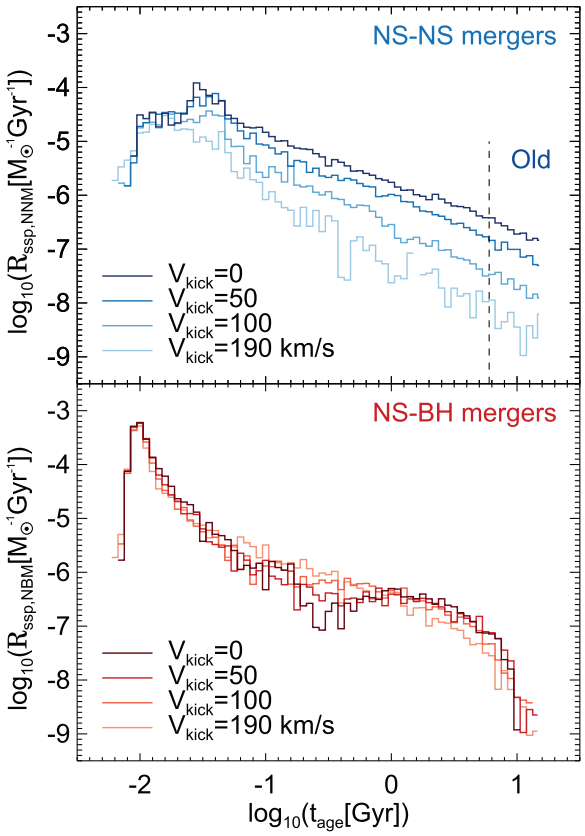

Figure 1. Event rates of NNM (upper panel) and NBM (lower panel) as a function of age for SSPs of 1 $M_\odot$ with solar metallicity in YUNNAN-II model. Lines of different colors indicate results with different $V_{\rm kick}$ as shown in the label. The vertical dashed line in the upper panel marks the age of 6 Gyr, which is the division of 'Old' NNM population: NNMs with merger timescale longer than 6 Gyr is defined as Old NNMs.

[3]The distribution of kick velocity of supernovae in stellar evolution model is generally fitted with a Maxwellian distribution. In this work, the parameter $V_{\rm kick}$ represents the dispersion of this Maxwellian distribution. $V_{\rm kick}$ applies to both the first and second supernovae during the formation of NNMs or NBMs. See appendix A1 of Hurley et al. (2002) for more details.

is beyond the scope of this paper. We leave this question in future works.

2.3 Calculating event rates

For an SSP,[4] during the running of the BSE algorithm as described in Section 2.2, we record every NNM and NBM event that occurs in the evolution process. By doing so, we get the COM event rate $\mathcal{R}_{\rm ssp,COM}(Z, t_{\rm age})$ for an SSP of certain age and metallicity.

For a galaxy that is comprised of millions to billions of stars with different mass, age, and metallicity, the total COM rate in a galaxy at a certain time t, $R_{\rm COM}(t)$, can be calculated as the sum of the COM rate for all the SSPs in the galaxy:

$$R_{\rm COM}(t) = \int \int_0^t SFR(Z,\tau)\,\mathcal{R}_{\rm ssp,COM}(Z, t-\tau)\,{\rm d}\tau{\rm d}Z, \quad (1)$$

where $SFR(Z, \tau)$ is the star formation rate of the galaxy at time τ for stars with metallicity Z, $\mathcal{R}_{\rm ssp,COM}(Z, t-\tau)$ is the COM rate for an SSP of mass $1\,{\rm M}_\odot$ with metallicity Z and age $t-\tau$.

In this work, we use the discretized version of equation (1) to calculate $R_{\rm COM}$ in a galaxy at time t:

$$R_{\rm COM}(t) = \sum_{i=0}^{N_{\rm SP}} M_{\rm i}\mathcal{R}_{\rm ssp,COM}\left(Z_{\rm i}, t - t_{\rm form,i}\right), \quad (2)$$

where $N_{\rm SP}$ is the total number of SSPs in this galaxy, and $M_{\rm i}$, $Z_{\rm i}$, $t_{\rm form,\,i}$ are the initial mass, metallicity, and formation time of the $\rm i_{th}$ SSP, respectively.

The observed event rate of kilonovae $R_{\rm kilonova}$ can be written as

$$\begin{aligned} R_{\rm kilonova} &= f_{\rm beam}(f_{\rm kilonova,NNM}R_{\rm NNM} + f_{\rm kilonova,NBM}R_{\rm NBM}) \\ &\le R_{\rm NNM} + R_{\rm NBM} = R_{\rm COM}. \end{aligned} \quad (3)$$

$R_{\rm NNM}$ and $R_{\rm NBM}$ are the event rates of NNMs and NBMs, respectively. $f_{\rm beam}$ is the beaming factor. As shown by Metzger & Berger (2012), the ejecta of kilonova has a rather isotropic structure and can be observed from a broad angle range. Therefore, we adopt $f_{\rm beam} = 1$ in this work. $f_{\rm kilonova,\,NNM}$ ($f_{\rm kilonova,\,NBM}$) is the fraction of NNMs (NBMs) which could trigger kilonovae. The values of $f_{\rm kilonova,\,NNM}$ and $f_{\rm kilonova,\,NBM}$ are still unclear. We assume all NNMs and NBMs can trigger kilonovae in this work, and $R_{\rm COM}$ should be treated as an upper limit of $R_{\rm kilonova}$.

Compared with NNM (see Baiotti & Rezzolla 2017 for a review), the mechanism and EM counterpart of NBM is much more ambiguous and still under debate. If the mass ratio of black hole over neutron star is very large, the neutron star will be swallowed into the black hole as a whole, and no EM emission is expected. Otherwise, the neutron star will be disrupted tidally beyond the Schwarzschild radius of the black hole and produce EM emission (Shibata et al. 2009). Besides, even in the large mass ratio case, if the neutron star is highly magnetized or the black hole is charged, certain EM emission could be produced (Mingarelli, Levin & Lazio 2015; D'Orazio et al. 2016; Dai 2019; Zhang 2019). On the observation side, several NBM candidates have been detected during the LVC O3. Among them, S190814bv is the most attracting one, as its FAR is 1 per 1.559×10^{25} yr. However, no EM counterpart of S190814bv has been found so far (Andreoni et al. 2019; Dobie et al. 2019; Gomez et al. 2019). The possible reasons may be that S190814bv is actually a BBM rather than an NBM, or the mass ratio of BH–NS is too large for EM emission as mentioned above. In summary, we assume all NNMs and NBMs can produce kilonovae for simplicity. Which kind of NBMs can produce kilonovae and the fraction of them are still unclear, both theoretically and observationally.

[4]An SSP represents a set of stars formed together at the same time, having the same age and metallicity. 'Simple' is used to be distinguished from the so-called complex stellar population, which is composed of multiple SSPs.

3 COM EVENT RATE AND R-PROCESS PRODUCTION

In this section, we show first the merger event rates of SSP for both NNMs and NBMs in the YUNNAN-II stellar population synthesis model. Then we study the cosmic COM rate density predicted in our GABE semi-analytic model, by combining the $\mathcal{R}_{\rm ssp,COM}$ of YUNNAN-II model with star formation histories using equation (2) for each galaxy. In Section 3.3, we present the amount of r-process elements produced by NNMs and NBMs in the lifetimes of galaxies.

3.1 Event rate in SSP

Fig. 1 shows the event rates, we derive from the YUNNAN-II stellar population synthesis model for SSPs, as a function of the age of the stellar population. $\mathcal{R}_{\rm ssp,NNM}$ and $\mathcal{R}_{\rm ssp,NBM}$ are event rates of NNMs and NBMs, and are presented in the upper and lower panels, respectively. In each case, results for four different values of supernovae kick velocities are shown, and are all for solar metallicity ($Z_\odot = 0.02$ in this work).

In the upper panel of Fig. 1, for $V_{\rm kick} = 0$ km s^{-1}, we see that NNMs start to appear at ~ 10 Myr after the birth of the stellar population. The event rate $\mathcal{R}_{\rm ssp,NNM}$ peaks at ~ 30 Myr and then decreases as $\propto t_{\rm age}^{-1}$, consistent with the theoretical expectation of the delay time distribution of COMs (Toonen, Nelemans & Portegies Zwart 2012; Yungelson 2013; Maoz, Mannucci & Nelemans 2014). For different $V_{\rm kick}$, $\mathcal{R}_{\rm ssp,NNM}$, in general, decreases as $V_{\rm kick}$ increases. The difference is small for $t_{\rm age} < 20$ Myr, and can be as large as 2 dex at late times.

In the lower panel of Fig. 1, we see that at all ages NBM event rates are similar for different values of $V_{\rm kick}$, except for the dip of $\mathcal{R}_{\rm ssp,NBM}$ with $V_{\rm kick} = 0$ km s^{-1} between 100 Myr $< t_{\rm age} <$ 1 Gyr. We have checked the model in detail and found two reasons responsible for such dependence of event rates on $V_{\rm kick}$: (1) In YUNNAN-II model, the supernova that leaves a black hole as its remnant does not have kick velocity to the binary system, while the supernova that forms a neutron star has natal kick. Therefore, changing $V_{\rm kick}$ has smaller influence on $\mathcal{R}_{\rm ssp,NBM}$ than on $\mathcal{R}_{\rm ssp,NNM}$. (2) For $V_{\rm kick} = 0$ km s^{-1}, $\mathcal{R}_{\rm ssp,NBM}$ peaks at ~ 10 Myr and also at ~ 1 Gyr. During the helium-burning regime of the secondary star of a binary, if the star overfills the Roche lobe, a common envelope forms. The orbital energy is then used to overcome the binding energy of common envelope, decreasing the separation tremendously. This NS–BH binary will coalesce in $\sim$ Myr, which corresponds to the peak at ~ 10 Myr. Otherwise, the secondary evolves to a neutron star independently and form an NS–BH binary with relatively large separation. The orbital energy is dissipated through GWs, and this NS–BH would coalesce in $\sim$ Gyr scale. Increasing $V_{\rm kick}$ extends the time-scales for mergers to happen, and makes the two peaks less distinct.

In Fig. 2, we show the dependence of $\mathcal{R}_{\rm ssp,COM}$ on metallicity for $V_{\rm kick} = 0$ km s^{-1}. We see that the event rates peak at earlier ages for higher metallicity, indicating shorter time-scales of mergers to happen. Nevertheless, the dependence on metallicity for both COM rates is relatively weak (less than about a magnitude), much less than the dependence on age.

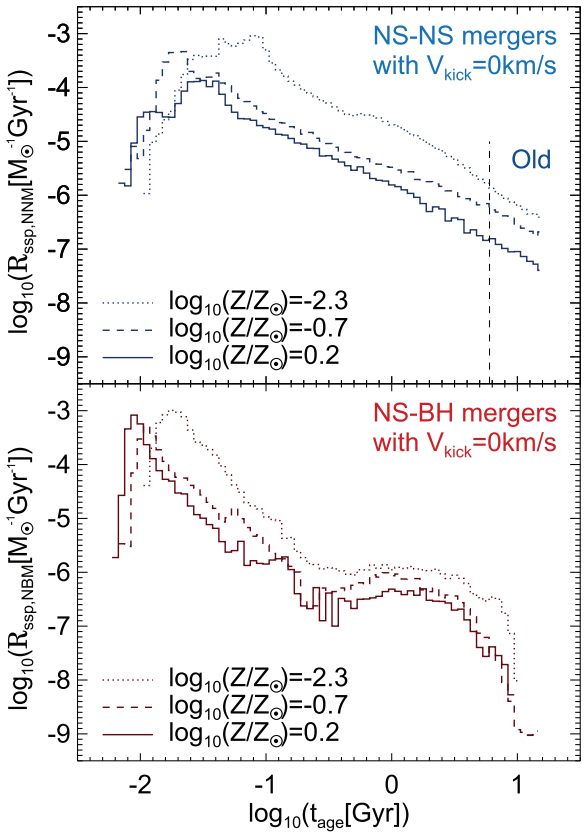

Figure 2. Event rates of NNM (upper panel) and NBM (lower panel) as a function of age for SSPs of 1 $M_\odot$ with different metallicities in YUNNAN-II model with $V_{\rm kick} = 0$ km s^{-1}. Lines of different line styles indicate results with different metallicities as shown in the label. The vertical dashed line in the upper panel marks the age of 6 Gyr, which is the division of 'Old' NNM population: NNMs with merger time-scale longer than 6 Gyr is defined as Old NNMs.

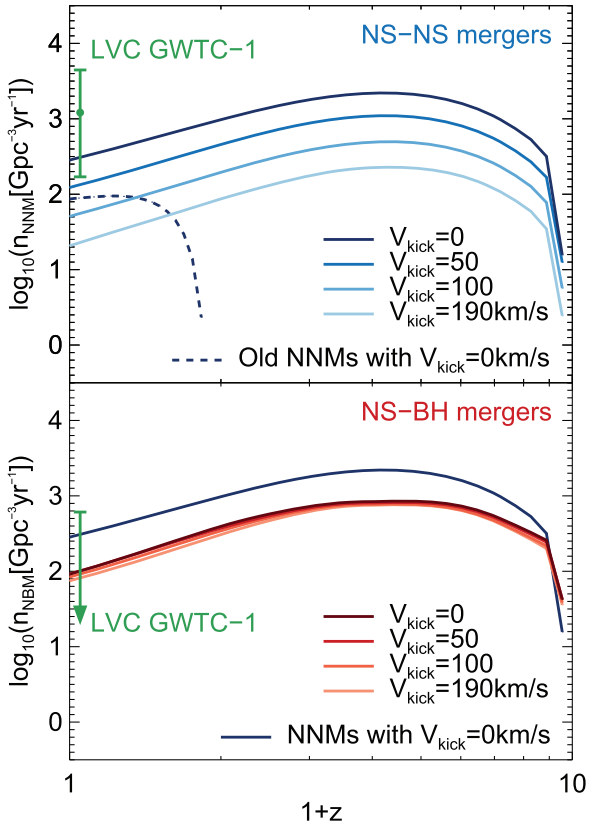

Figure 3. Upper panel: cosmic NNM event rate per comoving volume as a function of redshift. Solid lines with different colors represent results with different $V_{\rm kick}$ as shown in the label. The dashed blue line shows the event rate density of Old NNMs with $V_{\rm kick} = 0$. The green dot with error bar is the observational result of LVC GWTC-1 at $z \sim 0$ (Abbott et al. 2019a). Lower panel: the same as in the upper panel, but for NBMs. For comparison, the event rate density of NNMs with $V_{\rm kick} = 0$ is also shown as the blue solid line.

As mentioned in Section 1, the first directly detected NNM event is GW170817. The time-scale from star formation to coalescence of this binary is larger than 6.8 Gyr with 90 per cent confidence according to the stellar mass build-up history of its host galaxy NGC 4993, which is inferred from its best-fitting spectral energy distribution (SED) model (Blanchard et al. 2017). To be compared with this specific observed event and check whether GW170817 in NGC 4993 is a typical NNM event, we study, in particular, the 'Old' NNMs, defined as the NNMs that have survived longer than 6 Gyr before mergers happen, as shown in the upper panels of Figs 1 and 2. From these panels, we see that the 'Old' NNMs that are like GW170817 are only a small fraction ($\sim$ 14 per cent) of all NNMs. For NBMs, the lower panels of Figs 1 and 2 show that $\mathcal{R}_{\rm ssp,NBM}$ drops quickly in old SSPs ($>$ 10 Gyr), corresponding to few 'Old' NBMs predicted in the model.

3.2 Cosmic event rate density

In the previous subsection, we show COM event rates in SSPs. From this subsection, we will use the semi-analytic model to predict the total event rate from the cosmological point of view, including galaxies with different star formation histories comprised of complex stellar populations, using the method described in Section 2.3.

When accounting for all galaxies in the output of the semi-analytic model, Fig. 3 gives the cosmic COM rate density as a function of redshift, where results from the NNMs and NBMs are shown in the upper and lower panels, respectively. From the upper panel, we see that the NNM cosmic rate $n_{\rm NNM}$ peaks at $z \sim 3.3$ and decreases gradually towards $z = 0$, closely following the trend of the cosmic star formation rate density which peaks at $z \sim 3.6$ in GABE,[5] with a short time delay in general ($\sim$ 180 Myr). The time delay agrees with the delay time distribution of NNMs as shown in Fig. 1. With different $V_{\rm kick}$, $n_{\rm NNM}$ varies by a factor of $\sim$1 dex. The number density with $V_{\rm kick} = 0$ km s^{-1} at $z = 0$ is 283 Gpc^{-3} yr^{-1}, marginally agree with the observational result of LVC GWTC-1 (Abbott et al. 2019a), which is 1210^{+3230}_{-1040} Gpc^{-3} yr^{-1}, as shown by the green dot with error bar in the upper panel of Fig. 3. Results with higher $V_{\rm kick}$ predict

[5]It should be noted that the peak of $n_{\rm NNM}$ strongly depends on the peak of cosmic star formation history in our model. Recent observations favour that the cosmic star formation rate density peaked at $z \sim 2$ (summarized in Madau & Dickinson 2014), although the measurement of star formation at high redshifts suffers huge uncertainties. At present, GABE is only calibrated with observations at $z \sim 0$, and cannot recover the cosmic star formation rate at high redshift very well, so the peak of $n_{\rm NNM}$ could be lower than our prediction here and close to $z = 2$. This will be revisited in our future works. However, due to the short delay between star formation and COMs, this defect has little impact on the properties of NNMs and NBMs at $z \sim 0$ since our model of star formation in the low-redshift universe are well constrained by various observational facts.

Table 1. COM event rates in the model and in observation at $z = 0$. For NNMs, our model results of the cosmic COM rate density $n_{\rm COM}$ for four different $V_{\rm kick}$ are listed. LVC GWTC-1 (Abbott et al. 2019a) result is also listed for comparison. For NBMs, only results with $V_{\rm kick} = 0$ km s^{-1} are shown since the dependence of $n_{\rm NBM}$ on $V_{\rm kick}$ is weak. The three right columns list the event numbers per year predicted for different GW detectors in each case. $V_{\rm kick} = 0$ km s^{-1} is chosen as the fiducial model of this work and the related numbers are shown in bold.

	$V_{\rm kick}$ (km s^{-1})	$n_{\rm COM}$ (Gpc^{-3} yr^{-1})	$N_{\rm COM}$(yr^{-1}) Virgo	LIGO L1	LIGO H1
NNMs	**0**	**283**	**0.231**	**1.45**	**12.3**
	50	123	0.100	0.629	5.32
	100	51	0.041	0.26	2.2
	190	21	0.017	0.11	0.90
	LVC GWTC-1	1210^{+3230}_{-1040}	$0.99^{+2.64}_{-0.85}$	$6.21^{+16.57}_{-5.34}$	$52.5^{+140.2}_{-45.1}$
NBMs	**0**	**91**	**0.075**	**0.47**	**4.0**
	LVC GWTC-1	<610	<0.50	<3.13	<26.5

lower event rate densities, due to the generally lower event rate in SSP as shown in Fig. 1. Therefore, we choose $V_{\rm kick} = 0$ km s^{-1}, i.e. $n_{\rm NNM} = 283$ Gpc^{-3} yr^{-1}, as our fiducial model, which our following analysis is based on. Compared with other works before, our fiducial model falls into their plausible ranges (1.5−600 Gpc^{-3} yr^{-1}, Chruslinska et al. 2018; 20−600 Gpc^{-3} yr^{-1}, Mapelli & Giacobbo 2018; 238 Gpc^{-3} yr^{-1}, Artale et al. 2019).

Blue dashed line in the upper panel of Fig. 3 shows $n_{\rm NNM}$ of Old NNMs (as defined in Section 3.1) with $V_{\rm kick} = 0$ km s^{-1}. Old NNMs start to appear at low redshift ($z < 0.8$) when some stellar populations become older than 6 Gyr, and have a larger fraction in all NNMs towards lower redshift. At $z = 0$, Old NNMs is about 30 per cent of all NNMs. According to Blanchard et al. (2017), GW170817 is found in an old galaxy, and is probably an old NNM. While our result shows that younger NNMs have higher event rate density than Old NNMs in the local universe. More younger NNMs should be discovered (and in younger galaxies) with future observations, especially when GW detectors go to higher redshifts (the horizon of LIGO H1 during O2 is 218 Mpc, i.e. $z < 0.043$).

In the lower panel of Fig. 3, the evolution of the event rate density of NBMs, $n_{\rm NBM}$, is shown. The trend is similar as for the evolution of $n_{\rm NNM}$ shown in the upper panel, and also follows the trend of star formation rate density closely. The results do not vary much with different $V_{\rm kick}$, consistent with the results of SSPs as shown in the lower panel of Fig. 1. For $V_{\rm kick} = 0$ km s^{-1}, the NBM rate density is in general lower than the NNM rate density. At $z = 0$, $n_{\rm NBM}$ is 91 Gpc^{-3} yr^{-1}, about a third of $n_{\rm NNM}$, which is consistent with the upper limit proposed by LVC GWTC-1 shown as the green arrow.

The cosmic event rate densities at $z = 0$ for NNMs and NBMs in different models are listed in Table 1. We also show the event number per year that is predicted to be detected by Virgo and LIGO detectors, by assuming the detector horizons of NNMs and NBMs are 58, 107 and 218 Mpc for Virgo, LIGO L1 and LIGO H1, respectively (Abbott et al. 2017a).

Our models prefer a low kick velocity (< 50 km s^{-1}) for the progenitors of NNMs. Whereas, the observation of pulsar proper motions claim a much larger kick velocity: 190 km s^{-1} (Hansen & Phinney 1997), and 265 km s^{-1} (Hobbs et al. 2005). This inconsistency may shed some light on understanding the different formation routes of the isolated neutron stars and the ones in the pairs. Recent studies have proposed two formation channels for neutron stars with low kick velocity in binaries: (1) Podsiadlowski et al. (2004) found that stars with initial mass 8−11 M$_\odot$ in binary systems are likely to undergo an electron-capture supernova, rather than a neutrino-driven supernova as the case for a single star. Accretion induced collapse of massive white dwarfs with O/Ne/Mg cores can also lead to electron-capture supernovae. Electron-capture supernova is almost symmetric, short-duration and has smaller explosion energy (Dessart et al. 2006; Gessner & Janka 2018), which naturally leads to an explosion with smaller kick velocity. (2) Tauris et al. (2015), Tauris et al. (2017) concluded that ultrastripped supernovae (the second supernova in the formation of NS–NS and whose progenitor is an almost naked helium star) in close binaries generally have small kick velocities, due to the low mass (< 0.1 M$_\odot$) and low binding energy of the helium envelope. However, these channels have relatively strict requirement for the initial parameters of binaries. For instance, electron-capture supernova only works for stars with initial mass 8−11 M$_\odot$, and ultrastripped supernova require the pre-supernova orbital period to be 1 h−2 d. The fraction of ultrastripped supernovae of all supernovae Ic is small (< 1 per cent, Tauris et al. 2013).

Note that LVC GWTC-1 only constrains the merged NS–NSs, rather than the whole population. The initial conditions of such merged NS–NSs, as well as their evolutionary tracks and kick velocities, could be different from ones that not merged. It may be not appropriate to quantify kick velocities by using one parameter. A more refined and physical model for the determination of kick velocities may be needed. This is beyond the scope of this paper and we leave it to future works. More detection and better constraint from LVC O3 may also alleviate this inconsistency.

3.3 r-process elements production

The ejected neutron-rich wind during an NNM or NBM provides an excellent environment for r-process nucleosynthesis, which is a nuclear process responsible for the production of about half of the elements heavier than iron (Burbidge et al. 1957; Cameron 1957; Meyer 1994). The ejecta is extremely neutron-rich (with electron fraction ∼0.05), which allows nuclei to capture neutrons on a time-scale faster than β-decay, and some neutron-rich isotopes can only be produced through r-process. r-process elements can be produced not only in NNMs and NBMs, but may also be produced in core-collapse supernovae (Wheeler, Cowan & Hillebrandt 1998; Argast et al. 2004; Arnould, Goriely & Takahashi 2007) and high entropy winds from young neutron stars (Woosley & Hoffman 1992). In this work, we focus on the r-process in NNMs and NBMs, and do not account for all other possible formation and reduction channels.

We calculate the total r-process elements mass produced by NNMs and NBMs in a galaxy as

$$M_{\rm rp} = M_{\rm ejecta,NNM} N_{\rm life,NNM} + M_{\rm ejecta,NBM} N_{\rm life,NBM}, \quad (4)$$

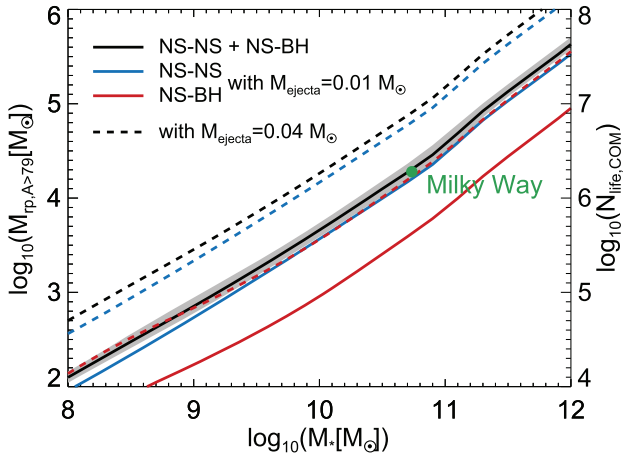

Figure 4. The mass of r-process elements with $A > 79$ in a galaxy, $M_{\rm rp,\,A>79}$, as a function of galaxy stellar mass at $z = 0$ in our fiducial model. The blue and red solid lines are median $M_{\rm rp,\,A>79}$ produced through NNM and NBM by assuming $M_{\rm ejecta,NNM} = M_{\rm ejecta,NBM} = 0.01\,{\rm M}_\odot$, while the black solid line shows the sum of the two, with grey shadow indicates 1σ scatter around the median. The dashed blue, red, and black lines are results when assuming $M_{\rm ejecta,NNM} = M_{\rm ejecta,NBM} = 0.04\,{\rm M}_\odot$. The y- axis, on the right-hand side, shows the corresponding number of COMs in the whole life of a galaxy, $N_{\rm life,\,COM}$, for the case of $M_{\rm ejecta,NNM} = M_{\rm ejecta,NBM} = 0.01\,{\rm M}_\odot$. The green dot is the amount of observed r-process elements of the Milky Way: $M^{\rm obs}_{\rm rp,A>79,MW} = X^{\rm obs}_{\rm A>79} M_{*,\rm MW} = 1.90^{+0.22}_{-0.21} \times 10^4\,{\rm M}_\odot$, with $X^{\rm obs}_{\rm A>79} = 35.0^{+0.4}_{-0.3} \times 10^{-8}$ (Arnould et al. 2007; Côté et al. 2018) and $M_{*,\rm MW} = (5.43 \pm 0.57) \times 10^{10}\,{\rm M}_\odot$ (McMillan 2017).

where $N_{\rm life,\,NNM}$ and $N_{\rm life,\,NBM}$ are the total number of NNMs and NBMs in the whole life of a galaxy, which are derived from GABE directly.

$M_{\rm ejecta,\,NNM}$ and $M_{\rm ejecta,\,NBM}$ are the mass of produced r-process elements in one NNM and NBM event, or the 'yield' of r-process elements. The uncertainties of the yields are huge. For NNMs with different neutron star masses, the ejecta masses can vary by a factor of 5, from 7.6×10^{-3} to $3.9 \times 10^{-2}\,{\rm M}_\odot$, and can be larger or smaller than the ones of NBMs (Korobkin et al. 2012). For NBMs with different black hole spin, the ejecta masses vary by a factor of ~200 (Bauswein et al. 2014). Besides, the equation of state of the neutron star, and detailed disc-ejecta configuration can also influence nucleosynthesis efficicy of NBMs by a factor of a few (Tanaka et al. 2014; Fernández et al. 2017). Here, in this work, for simplicity, we assume that NNMs and NBMs have the same yield, and are the same as the observational constrains of the ejecta mass of GW170817 (Côté et al. 2018).[6] The value we adopt is $M_{\rm ejecta,NNM} = M_{\rm ejecta,NBM} = 0.01{-}0.04\,{\rm M}_\odot$, for r-process elements with $A > 79$.

Fig. 4 gives the total mass of r-process elements with $A > 79$ in a galaxy, $M_{\rm rp,\,A>79}$, as a function of galaxy stellar mass at $z = 0$ in our fiducial model. The solid and dashed lines are the predicted $M_{\rm rp,\,A>79}$ by assuming $M_{\rm ejecta,NNM} = M_{\rm ejecta,NBM} = 0.01\,{\rm M}_\odot$ and $M_{\rm ejecta,NNM} = M_{\rm ejecta,NBM} = 0.04\,{\rm M}_\odot$, respectively, representing the lower and upper limits of our model prediction. The $M_*{-}M_{\rm rp,\,A>79}$ relation follows a power law with a scatter of only ~0.2 dex,

[6]Their tables 1 and 2 are compilations of various literatures (Perego et al. 2014; Arcavi et al. 2017; Chornock et al. 2017; Cowperthwaite et al. 2017; Evans et al. 2017; Kasen et al. 2017; Kasliwal et al. 2017; Nicholl et al. 2017; Smartt et al. 2017; Tanaka et al. 2017; Tanvir et al. 2017; Troja et al. 2017; Abbott et al. 2017c; Rosswog et al. 2018).

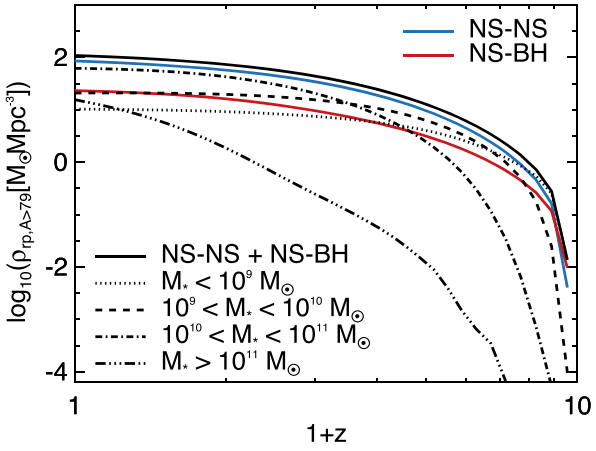

Figure 5. Cosmic amount of r-process elements with $A > 79$ in galaxies per comoving volume, $\rho_{\rm rp,\,A>79}$, as a function of redshift in our fiducial model, and with $M_{\rm ejecta,NNM} = M_{\rm ejecta,NBM} = 0.01\,{\rm M}_\odot$. The blue and red solid lines are the results of NNMs and NBMs, respectively, and the black solid line is the sum of both channels. Black lines with different line styles are the amount of r-process elements contributed by galaxies with different stellar mass ranges, as shown in the label.

indicating that stellar mass determines the mass of r-process elements predominantly, much more than colors, star formation rates, metallicities, morphology, etc. The contributions from NNMs and NBMs are ~ 80 and ~ 20 per cent at almost all stellar masses.

By adopting the r-process mass fraction in the solar r-process residual, $X^{\rm obs}_{\rm A>79} = 35.0^{+0.4}_{-0.3} \times 10^{-8}$ (Arnould et al. 2007; Côté et al. 2018), and the Milky Way mass, $M_{*,\rm MW} = (5.43 \pm 0.57) \times 10^{10}\,{\rm M}_\odot$ (McMillan 2017), the observed mass of r-process elements in the Milky Way is $M^{\rm obs}_{\rm rp,A>79,MW} = X^{\rm obs}_{\rm A>79} M_{*,\rm MW} = 1.90^{+0.22}_{-0.21} \times 10^4\,{\rm M}_\odot$, as indicated by the green dot in Fig. 4. This observed value is in good agreement with our model prediction of $M_{\rm ejecta} = 0.01\,{\rm M}_\odot$, which is $M_{\rm rp,A>79,MW} = 2.0^{+0.5}_{-0.4} \times 10^4\,{\rm M}_\odot$ for Milky Way-mass galaxies (with $N_{\rm life,COM,MW} = 2.0^{+0.5}_{-0.4} \times 10^6$). The model of $M_{\rm ejecta} = 0.04\,{\rm M}_\odot$ (dashed lines) overestimates the amount of r-process elements in Milky Way-mass galaxies. If the yield is indeed $0.04\,{\rm M}_\odot$, NBMs alone can provide sufficient amount of r-process elements in the Milky Way (the red dashed line).

In Fig. 5, we show the cosmic density evolution of the amount of r-process elements with $A > 79$ predicted in our model. Only the model with $M_{\rm ejecta,NNM} = M_{\rm ejecta,NBM} = 0.01\,{\rm M}_\odot$ is shown here, considering that adopting a different yield would not change the general trend of the result. As stellar mass is a good indicator of r-process elements as seen in Fig. 4, the amount of r-process elements accumulated gradually as the universe evolves towards low redshift. About 50 per cent of r-process elements nowadays already existed at $z \sim 1.6$, and about 90 per cent r-process elements nowadays formed before $z \sim 0.3$. The contributions from NNMs and NBMs are always ~ 80 per cent and ~ 20 per cent respectively, except for the earliest redshifts, due to the fact that NBMs have higher event rate than NNMs in young stellar populations (as shown in Fig. 1). We also explore the amount of r-process elements in galaxies with different stellar masses, as shown by black lines with different line styles. At $z = 0$, most r-process elements (~ 57 per cent) are stored in galaxies with $10 < \log(M_*[\,{\rm M}_\odot]) < 11$, which means Milky Way-mass galaxies are the main sites for historical r-process nucleosynthesis.

Our fiducial model ($n_{\rm NNM} = 283\ {\rm Gpc^{-3}\ yr^{-1}}$ and $n_{\rm NBM} = 91\ {\rm Gpc^{-3}\ yr^{-1}}$) with $M_{\rm eject} = 0.01\,{\rm M}_\odot$ matches the observed abundance of the Milky Way very well. Note that we have only calculated

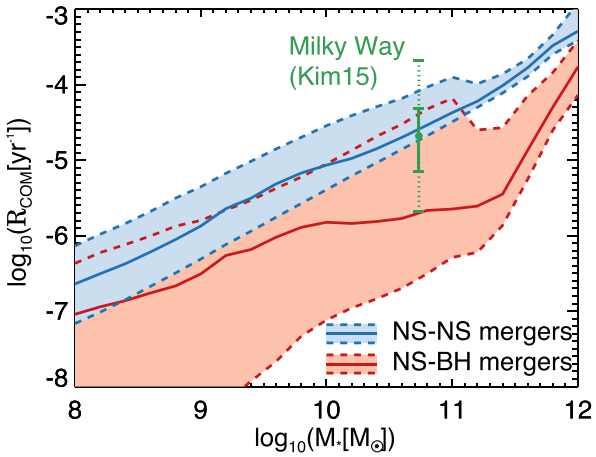

Figure 6. The total event rates of NNMs and NBMs in a galaxy, as a function of galaxy stellar mass at $z = 0$ in our fiducial model. The solid lines show the median relations (blue for NNMs and red for NBMs). The light colour regions and dashed lines indicate the 1σ scatter. The green dot with solid error bars is the observational result of Kim, Perera & McLaughlin (2015) for the NNM rate in the Milky Way, and the dotted error bars present the uncertainty after considering different assumptions about the pulsar luminosity distribution (Chruslinska et al. 2018).

the r-process nucleosynthesis through NNMs and NBMs in the model. On the other hand, heavy elements abundances are usually measured through meteorite, solar spectra, and stellar spectra (e.g. Anders & Grevesse 1989; Kappeler, Beer & Wisshak 1989), which are all in stellar component. However, a substantial fraction of heavy elements could stay in gas phase, which may cause the underestimation of heavy elements production efficiency in current observation. Besides, due to the spread delay time distribution of NNMs, the lifetime of some NS–NSs can be comparable with the age of the Universe. Thus, the offset between the location of coalescence and star-forming region can be ≥ 20 kpc (Fong & Berger 2013), which would also lower the amount of observed heavy elements leaving in galaxies.

4 PROPERTIES OF COM HOST GALAXY

4.1 Stellar mass and age

Fig. 6 shows the total event rates of NNMs and NBMs in a galaxy as a function of galaxy stellar mass at $z = 0$ in our fiducial model with $V_{\rm kick} = 0$ km s^{-1}. The median of the M_*–$R_{\rm NNM}$ relation can be well fitted by a power law, while M_*–$R_{\rm NBM}$ deviates from a single power law and has larger scatter. Compared with NNMs, there are more NBMs in young SSPs ($t_{\rm age} < 20$ Myr, as shown in Fig. 1). Therefore, $R_{\rm NBM}$ is more sensitive to recent star formation activities, which results in larger scatter.

The observational result of Kim et al. (2015) for the NNM rate in the Milky Way (21^{+28}_{-14} Myr^{-1}) is shown as the green dot with error bars in Fig. 6. At the Milky Way mass of $M_{*,\rm MW} = 5.43 \times 10^{10}$ M$_\odot$ (McMillan 2017), the predicted $R_{\rm NNM}$ in our model is $R_{\rm NNM,MW} = 25.7^{+59.6}_{-7.1}$ Myr^{-1}, in good agreement with the observation. The predicted $R_{\rm NBM}$ for Milky Way-like galaxies is much lower, with $R_{\rm NBM,MW} = 2.1^{+40.3}_{-1.8}$ Myr^{-1}.

As seen in Fig. 2, age influences COM event rate the most for SSP, so we check also the dependence of $R_{\rm COM}$ on the age of host galaxies.[7] In the left-hand column of Fig. 7, the distributions of COM event rates in galaxies at $z = 0$ of our fiducial model are plotted, in the stellar mass–galaxy age plane. The upper left-hand panel is the result of $R_{\rm NNM}$, which shows that massive/young galaxies generally have higher $R_{\rm NNM}$ than small/old galaxies, consistent with expectation as young stellar populations have higher event rate. The distribution can be divided into two populations as shown by the dotted line: for old galaxies above the line, there is almost no dependence on age; for galaxies younger, there exists clear dependence on both stellar mass and age.

The distribution of event rates for Old NNMs is shown in the middle left panel of Fig. 7. For the youngest galaxies with $t_{\rm age} < 2$ Gyr, the event rates of Old NNMs are always low, independent of galaxy stellar mass. For galaxies with $t_{\rm age} > 2$ Gyr, $R_{\rm NNM}$ of Old NNMs have strong dependence on stellar mass but almost no dependence on age. Compared with the case for all NNMs, the old galaxies above the dotted line in the upper left panel is mainly contributed by Old NNMs. The distribution of $R_{\rm NBM}$ is shown in the lower left panel of Fig. 7, which has similar trend as that of $R_{\rm NNM}$, except that without Old NBMs as shown in Section 3.1, the distribution of $R_{\rm NBM}$ always depends both on age and stellar mass.

The independence of Old NNMs event rate on galaxy age comes from its logarithmic delay time distribution. As shown in the upper panel of Fig. 1, the event rate of Old NNMs in SSPs of 1 M$_\odot$ with solar metallicity and $V_{\rm kick} = 0$ km s^{-1} spans 0.4 dex, from $10^{-6.4}$ to $10^{-6.8}$ M$_\odot^{-1}$ Gyr^{-1}. While the event rate of younger NNMs spans 2.5 dex, from $10^{-3.9}$ to $10^{-6.4}$ M$_\odot^{-1}$ Gyr^{-1}. As a result, Old NNMs have much weaker dependence on galaxy age than younger NNMs. We need to note that the division of these two populations in Figs 1 and 7 is for a better comparison with the observed unique case and an emphasize of the dependence of NNMs on the age of host galaxies: long merger time-scale NNMs are almost everywhere in the universe, except in the youngest galaxies ($t_{\rm age} < 2$ Gyr).

In the middle column of Fig. 7, we show the distribution of specific event rate defined as $R_{\rm COM}$ divided by stellar mass. The dependence on stellar mass is largely reduced in this case. For both NNMs and NBMs, the specific event rate is slightly higher for less massive galaxies at given galaxy age. This is because low-mass galaxies tend to have lower metallicity, while low-metallicity results in relatively higher $\mathcal{R}_{\rm ssp,COM}$ as shown in Fig. 2.

In order to compare our results with observation, we need to figure out the probability to observe a COM event in a sub-population of galaxies, considering the number density of galaxies into account. We calculate the probability to detect a sub-population of galaxies as the host galaxy of a COM event as

$$P_{\rm COM,i} = \frac{R_{\rm COM,i} N_{\rm gal,i}}{\sum_i R_{\rm COM,i} N_{\rm gal,i}}, \quad (5)$$

where the subscript i stands for a sub-population of galaxies, e.g. galaxies with given age and stellar mass (or other properties). $R_{\rm COM,\,i}$ is the mean COM rate and $N_{\rm gal,\,i}$ is the spatial number density of these galaxies. For example, the number densities of galaxies with certain stellar mass and age are presented in Fig. A1 for GABE (see Appendix A for details). Note that in this work we do not consider the selection effect in observations, and assume all the host galaxies of COMs can be observed, which may overestimate the number of

[7]The age of a galaxy in this work is the so-called 'mass weighted age', i.e. the mean value of ages of all the SSPs, weighted by the initial mass of each stellar population.

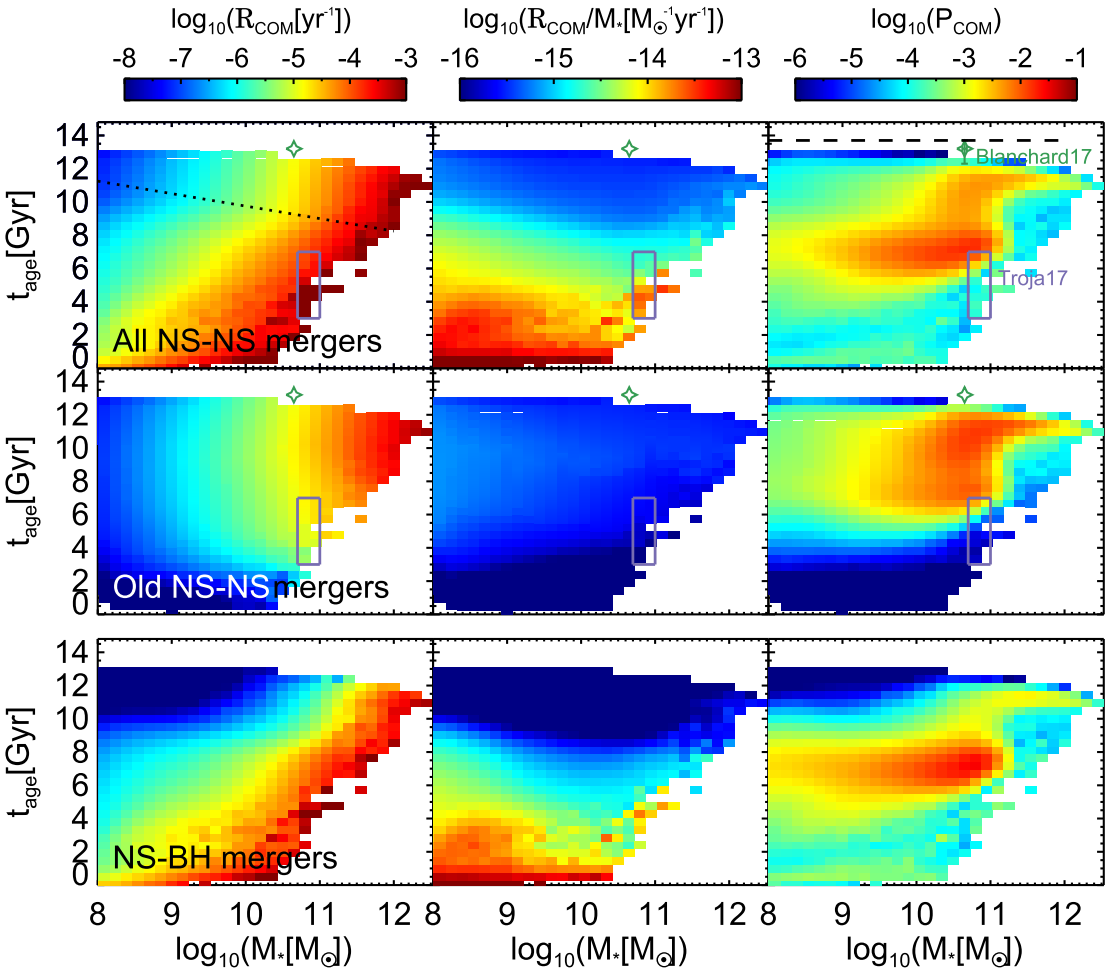

Figure 7. Distributions of event rate as a function of galaxy stellar mass and age at $z = 0$ in our fiducial model. Columns from the left- to right-hand side show results of: the COM rate, COM rate per stellar mass, and $P_{\rm COM}$ [the probability to observe a merger event in a sub-population of galaxy as defined by equation (5)]. The upper panels and middle panels are distributions of all NNMs and Old NNMs, respectively, and the bottom panels are results of NBMs. In each panel, colors show the mean value for galaxies in each cell as indicated in the colour bars. The dotted line in the upper left-hand panel is $t_{\rm age}[\,{\rm Gyr}] = -0.75 \times \log(M_*[\,{\rm M}_\odot]) + 17.25$, which divides the distribution into two populations. The green star represents NGC 4993, the host galaxy of GW170817, with $M_* = 4.47 \times 10^{10}\,{\rm M}_\odot$ and $t_{\rm age} = 13.2\,{\rm Gyr}$ (Blanchard et al. 2017), with error bar only shown in the upper right panel. The purple rectangle also represents NGC 4993, but is the observational result of Troja et al. (2017), with $M_* = (5-10) \times 10^{10}\,{\rm M}_\odot$ and $t_{\rm age} = 3-7\,{\rm Gyr}$. The dashed line in the upper right panel is $t_{\rm age} = 13.7\,{\rm Gyr}$, representing the age of the Universe.

small host galaxies. The influence of selection effect will be explored in future works.

The predicted distributions of $P_{\rm COM}$ as a function of stellar mass and age are shown in the right-hand column of Fig. 7. We find that galaxies with $M_* = 10^{10.65}\,{\rm M}_\odot$ and $t_{\rm age} = 7.1\,{\rm Gyr}$ are most likely detected as the host of an NNM event, as well as of an NBM. In the upper right-hand panel of Fig. 7, compared with the observational results of NGC 4993, the host galaxy of GW170817 (green star: Blanchard et al. 2017, hereafter Blanchard17; purple rectangle: Troja et al. 2017, hereafter Troja17), we see that the peak of our prediction is marginally consistent with Troja17. Blanchard17 gives similar stellar mass, but the age is much older (close to the age of the Universe, as represented by the horizontal dashed line).

By integrating $P_{\rm COM}$ along $t_{\rm age}$ (M_*), we can derive the stellar mass (age) distribution of the host galaxy of COMs, and the results are shown in Fig. 8 (Fig. 9). From Fig. 8, we see that the distributions of host galaxies of both NNMs and NBMs peak at around $10^{10.65}\,{\rm M}_\odot$, decreasing fast towards low-mass end and even faster towards high-mass end. The contribution of Old NNMs is about ~ 20 per cent for galaxies with $M_* < 10^{10}\,{\rm M}_\odot$. For more massive galaxies, Old NNMs contribute more, with a fraction as high as ~ 70 per cent. The observational results of Blanchard17 and Troja17 of NGC 4993 are shown by green and purple shadow in Fig. 8, both lying around the peak of the model prediction.

As presented in Fig. 9, the age distribution of host galaxies of NNMs is bimodal, with two peaks of around $t_{\rm age} = 7.1$ and $t_{\rm age} = 11.0\,{\rm Gyr}$. The latter is mainly contributed by Old NNMs. Observationally, the age provided by Blanchard17 and Troja17 differs a lot from each other, which reflects the huge systematic uncertainties in determining age through galaxy spectrum. Compared with the bimodal distribution of NNMs, the distribution of NBMs has a much weaker old peak ($t_{\rm age} \sim 11.0\,{\rm Gyr}$), because there is few Old NBMs in YUNNAN-II model.

The main results of this subsection is that young and massive galaxies have higher COM rate. The age dependence is mainly caused by young COMs. Considering number densities of galaxies into account, COMs are most likely to be observed in galaxies with $M_* \sim 10^{10.65}\,{\rm M}_\odot$ and $t_{\rm age} \sim 7.1$ and $11.0\,{\rm Gyr}$.

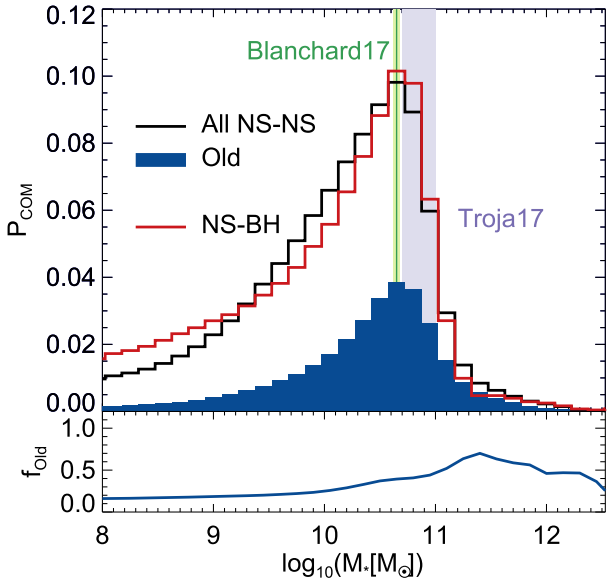

Figure 8. Upper panel: the stellar mass distribution of host galaxies of NNMs (black solid line) and NBMs (red solid line) at $z = 0$ in our fiducial model. The blue area gives the contribution of Old NNMs. The green and purple regions represent the observed stellar mass of NGC 4993 by Blanchard17 and Troja17, respectively. Lower panel: the fraction of Old NNMs over all NNMs as a function of stellar mass: $f_{\rm Old} = P_{\rm NNM,\,Old}/P_{\rm NNM}$.

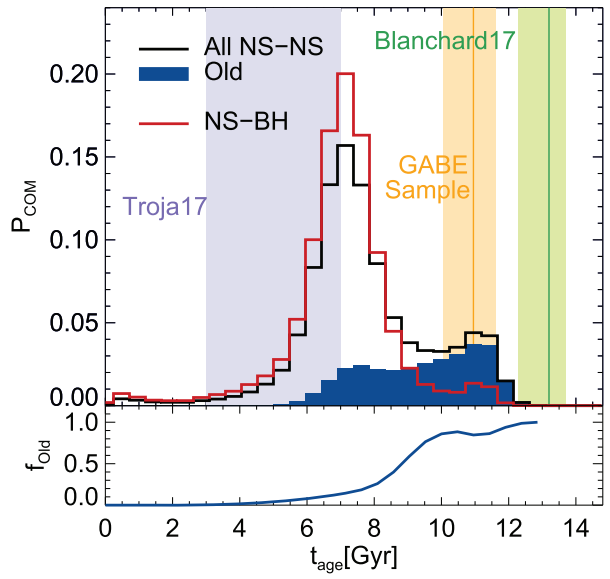

Figure 9. Upper panel: the age distribution of host galaxies of NNMs (black solid line) and NBMs (red solid line) at $z = 0$. The blue area is the contribution of Old NNMs. The green and purple regions represent the observed age of NGC 4993 provided by Blanchard17 and Troja17, respectively. The orange line and area are the predicted median and 1σ scatter of the age of selected NGC 4993-like galaxies in GABE catalogue, which is described in detail in Section 4.2. Lower panel: the fraction of Old NNMs over all NNMs as a function of galaxy age.

4.2 Colors, sSFR, metallicity and morphology

Following the analysis on galaxy stellar mass and age as shown in Figs 7–9, in this subsection, we further explore the dependence of $P_{\rm COM}$ on colour, specific star formation rate (sSFR), gas-phase metallicity and morphology (represented by bulge-to-total stellar mass ratio, $f_{\rm B/T} = M_{*,\,\rm bulge}/(M_{*,\,\rm bulge} + M_{*,\,\rm disc})$) for host galaxies of COMs. The results are presented in Figs 10 and 11. The upper three rows of Fig. 10 show the distribution of event rate in a galaxy ($R_{\rm NNM}$), normalized galaxy spatial number density ($P(n_{\rm gal})$) and detection probability ($P_{\rm NNM}$, as defined in equation (5)) for NNMs, on the planes of galaxy properties and galaxy stellar mass. For NBMs, only the distributions of $P_{\rm NBM}$ are shown in the bottom row of Fig. 10 for simplicity. They share similar distributions with that of NNMs host galaxies for all properties investigated.

By Integrating $P_{\rm COM}$ along stellar mass, we can derive the distributions of colour, sSFR, metallicity, and morphology for COM host galaxies in our model, as shown in Fig. 11. The distributions of colour, sSFR and morphology have two peaks, a red/quiescent/early-type sequence, and a blue/star-forming/late-type sequence that includes more galaxies, for both NNMs and NBMs. *Therefore it is more likely to detect COMs in blue/star-forming/late-type galaxies.* As expected, Old NNMs contribute more in red/quiescent/early-type sequence of all NNMs. The gas metallicity has a wide distribution and peaks at around 8.72−8.85, which is comparable to solar metallicity (the $Z_\odot = 0.02$ solar metallicity in unit of $12 + \log({\rm O/H})$ is 8.7). Old NNMs contribute more in metal-rich galaxies.

From the first row of Fig. 10, we can see that galaxies with more massive stellar mass, bluer colour, higher sSFR and lower metallicity tend to have higher NNM event rates. Compared with elliptical galaxies with equivalent stellar mass, spiral galaxies have slightly higher NNM event rates. There is no bimodality in the distributions of event rate. The bimodality of the colour, sSFR, and morphology distributions of $P_{\rm COM}$ (the third and fourth row of Figs 10 and 11) inherit from the bimodality of their number density distributions (the second row of Fig. 10). (1) In the number density distribution of $g - i$ colour, the split of two well-known populations is clear: red sequence and blue cloud. (2) In the number density distribution of sSFR, the star-forming main-sequence lies around 10^{-10} yr^{-1}, agree with the observational result of *GALEX* and SDSS (e.g. Salim et al. 2007). For galaxies with little star formation less than 10^{-13} yr^{-1}, the uncertainty on measuring their sSFR is large in observations and is not well determined (see fig. 15 in Salim et al. 2007). In our model, although the sSFR could be estimated accurately even it goes down to 10^{-20} yr^{-1}, for modelled galaxies with sSFR lower than 10^{-13} yr^{-1}, we set their sSFR to be 10^{-13} yr^{-1} for visualization purpose. These galaxies actually represent exhausted galaxies with almost no star formation. Because the number of these completely dead galaxies is not a small number, we could see the probability of NNM and NBM events in these galaxies is also not small. As a comparison, the sSFR of NGC 4993 is $10^{-12.65}$ yr^{-1}, i.e. there is almost no star formation inside. (3) Normally the morphology of galaxies is described by the ratio of their bulge mass and their total stellar mass in the disc and bulge ($f_{\rm B/T} = M_{\rm bulge}/(M_{\rm bulge} + M_{\rm disc})$). As $M_{\rm bulge}$ and $M_{\rm disc}$ are close to zero for pure-disc galaxies and elliptical galaxies respectively, the $f_{\rm B/T}$ of these two big famous popular populations are close to zero and unit, respectively ($f_{\rm B/T} < 0.03$ for pure-disc galaxies, and $f_{\rm B/T} > 0.7$ for elliptical galaxies). This is the reason we have many NNMs and NBMs crowed in these two end bins (populations).

For NGC 4993 that is observed to host GW170817, we list in Table 2 its properties derived by Blanchard17 and Troja17, and overplot the values from Blanchard17 in Figs 10 and 11 to be compared with model predictions. The observed values are always at or close to the peaks of the model distributions.

As listed in Table 2, the observed stellar mass, colour, and metallicity of NGC 4993 have small errors, much smaller than that of age and sSFR. Based on these 'accurate' properties, we define elliptical galaxies ($f_{\rm B/T} > 0.9$) with $M_* = 10^{10.5}$−$10^{10.8}$ M$_\odot$, $g - i =$

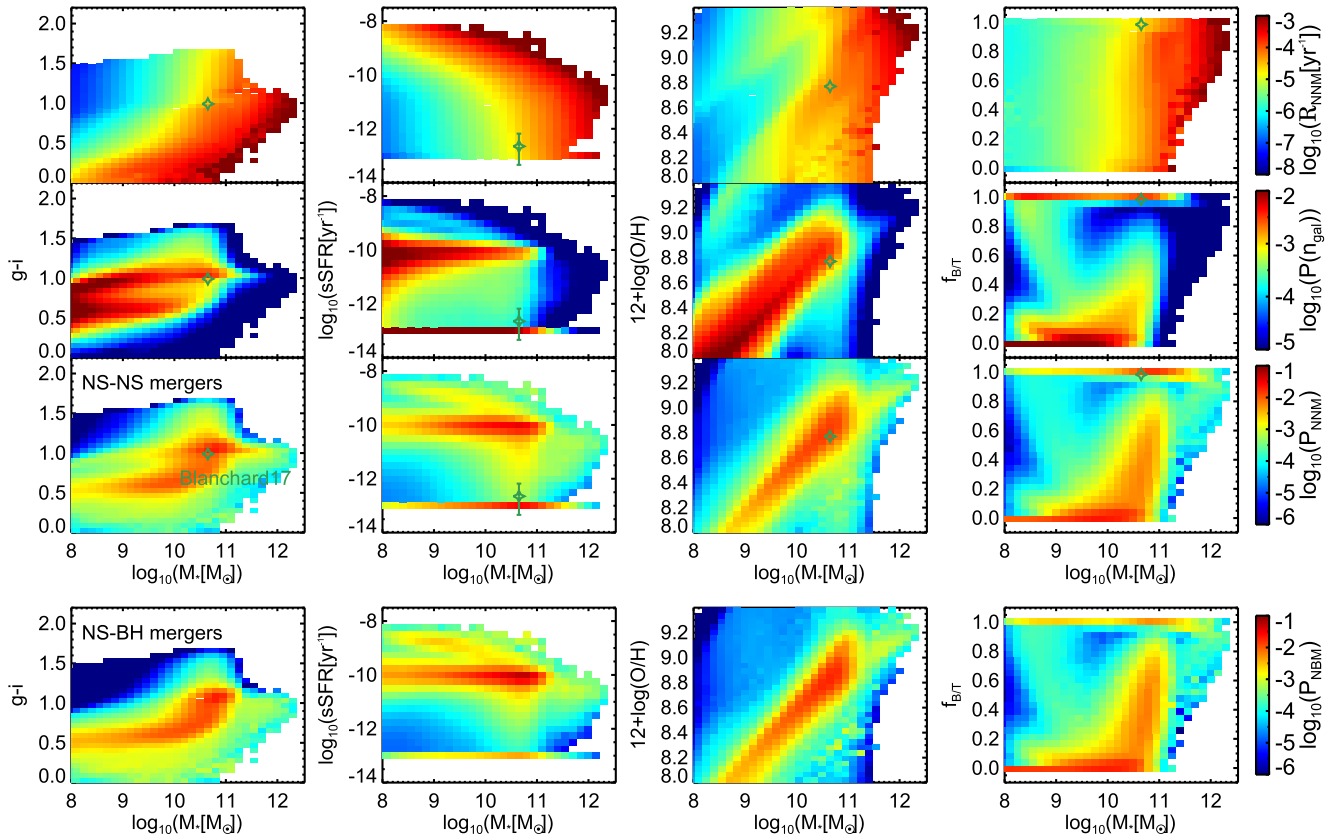

Figure 10. Upper three rows are for NNMs: the distributions of NNM event rate in a galaxy ($R_{\rm NNM}$), normalized galaxy spatial number density ($P(n_{\rm gal})$) and detection probability ($P_{\rm NNM}$, as defined in equation 5) are presented as a function of stellar mass and other properties of host galaxies (from the left- to the right-hand side, including $g-i$ colour, sSFR, gas-phase metallicity, and bulge-to-total stellar mass ratio ($f_{\rm B/T}$)) at $z=0$. For NBMs, only the distributions of $P_{\rm NBM}$ are shown in the fourth row for simplicity. Colors show the mean value in each cell as indicated in the colour bar. The green stars with error bar represent the observational result of NGC 4993 in Blanchard17, as listed in Table 2.

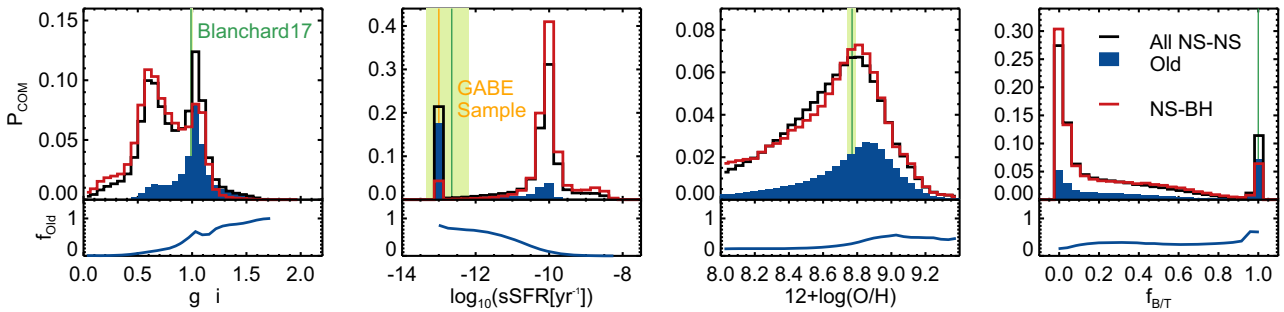

Figure 11. $g-i$ colour, sSFR, gas-phase metallicity, and $f_{\rm B/T}$ distributions of COM host galaxies at $z=0$, which are derived by integrating the distributions of $P_{\rm NNM}$ and $P_{\rm NBM}$ in Fig. 10 along stellar mass. The black and red lines are the distributions for NNMs and NBMs, respectively. Blue regions are the contribution of Old NNMs. The green area represents the observational result of NGC 4993 of Blanchard17, as listed in Table 2. The orange line is the predicted median sSFR of selected NGC 4993-like galaxies in GABE catalogue, which is 10^{-13} yr^{-1}. Lower panels in each column show the fraction of Old NNMs over all NNMs in each bin: $f_{\rm Old}=P_{\rm NNM,\,Old}/P_{\rm NNM}$.

$0.95-1.05$ and $12+\log({\rm O/H})=8.7-8.9$ as NGC 4993-like galaxies. We find 7604 such galaxies from GABE galaxy catalogue at $z=0$, and construct an NGC 4993-like galaxies sample. Their median age and 1σ scatter is $10.95^{+0.68}_{-0.90}$ Gyr, as shown by the orange region in Fig. 9, which locates right at the old peak of the model predicted distribution, closer to the result of Blanchard17 than that of Troja17. In total, 95 per cent of the selected NGC 4993-like galaxies have little star formation. Their median sSFR is 10^{-13} yr^{-1}, as shown by the orange line in Fig. 11.

5 CONCLUSION

In this work, we use the semi-analytic model of galaxy formation GABE, which includes modelling of binary evolution by adopting YUNNAN-II stellar population synthesis model to derive the NNM and NBM event rates for different kinds of galaxies. After presenting the NNM and NBM event rates in different SSPs predicted by the YUNNAN-II model, we study the predicted cosmic NNM and NBM event rate density, r-process elements produced through these

Table 2. Properties of NGC 4993. Observational results given by Blanchard17 and Troja17 are listed, including stellar mass, mass-weighted age from spectrum analysis, $g-i$ colour, sSFR, and gas-phase metallicity in unit of $12+\log(\mathrm{O/H})$ (transferred from the [Fe/H] in Blanchard17). The last column is NGC 4993-like galaxies selected from GABE galaxy catalogue, according to galaxy stellar mass, $g-i$ colour and metallicity as listed in this table. The predicted age and sSFR of selected NGC 4993-like galaxies are also listed and marked in bold.

Property	Blanchard17	Troja17	GABE sample
$\log(M_*/\mathrm{M}_\odot)$	$10.65^{+0.03}_{-0.03}$	10.7−11.0	10.5−10.8
age(Gyr)	$13.2^{+0.5}_{-0.9}$	3−7	$10.95^{+0.68}_{-0.90}$
$g-i$	$0.99^{+0.01}_{-0.01}$	–	0.95−1.05
$\log(\mathrm{sSFR}/\mathrm{yr}^{-1})$	$-12.65^{+0.47}_{-0.69}$	–	−13
$12+\log(\mathrm{O/H})$	$8.77^{+0.02}_{-0.02}$	–	8.7−8.9

mergers, and the properties of host galaxies of the mergers. Here, are the main results:

(i) In YUNNAN-II stellar population synthesis model that models binary evolution, the value of natal kick velocity of supernovae $V_{\rm kick}$ assumed in the model affects the NNM rates in SSPs, and also affect the cosmic NNM rate density, by as much as one magnitude, when changing the value from 190 to 0 km s^{-1}. The cosmic NNM rate density predicted with $V_{\rm kick}=0$ km s^{-1} (which we choose as the fiducial model) fits the observational result of LIGO Scientific Collaboration and Virgo Collaboration (LVC) best. However, the observation of single pulsar proper motions claims a much larger kick velocity (190 km s^{-1}, Hansen & Phinney 1997). This inconsistency may indicate that the evolutionary tracks and kick velocities of neutron stars in binary systems could be different from single neutron stars, and a more refined and physical model for kick velocities in binary evolution may be needed. Note that we have not done the full exploration of parameter space, which is beyond the scope of this work. Thus this result should be treated with caution. In our model, NNMs prefer to originate from binary systems with low kick velocities. Whereas, the NBM event rate density is almost independent of value of kick velocity in our model.

(ii) The predicted cosmic NNM events rate density at $z=0$ of our fiducial model is 283 Gpc^{-3} yr^{-1}, marginally in agreement with the value constrained by LVC GWTC-1 (1210^{+3230}_{-1040} Gpc^{-3} yr^{-1}). The NNMs that have similar old age as GW170817 are about 30 per cent of all NNMs at $z=0$. We expect that more NNMs in young galaxies should be observed in the future. The predicted cosmic event rate density of NBMs at $z=0$ of our fiducial model is 91 Gpc^{-3} yr^{-1}, about a third of the one of NNMs, which is also consistent with the upper limit proposed by LVC GWTC-1 (610 Gpc^{-3} yr^{-1}).

(iii) The predicted total number of NNMs and NBMs in the whole life of a Milky Way-mass galaxy is $2.0^{+0.5}_{-0.4}\times10^6$. By assuming yield mass $M_{\rm ejecta,NNM}=M_{\rm ejecta,NBM}=0.01\,\mathrm{M}_\odot$, the corresponding amount of r-process elements with $A>79$ is $2.0^{+0.5}_{-0.4}\times10^4\,\mathrm{M}_\odot$, comparable to the observational constraint ($1.90^{+0.22}_{-0.21}\times10^4\,\mathrm{M}_\odot$). Milky Way-mass galaxies are the main sites for historical r-process nucleosynthesis.

(iv) For a Milky Way-mass galaxy at $z=0$, the predicted NNM rate is $25.7^{+59.6}_{-7.1}\,\mathrm{Myr}^{-1}$, in a good agreement with the observational result of the Milky Way ($21^{+28}_{-14}\,\mathrm{Myr}^{-1}$, Kim et al. 2015). In general, young, and massive galaxies have higher NNM and NBM rate. NNMs and NBMs are most possible to be detected in galaxies with $M_*\sim10^{10.65}\,\mathrm{M}_\odot$ and metallicity of $12+\log(\mathrm{O/H})=8.72-8.85$, and are more in young, blue, star-forming, and disc galaxies. The properties of NGC 4993, the host galaxy of GW170817, are mostly at or near the peaks of model predicted distributions, indicating that NGC 4993 is a typical host galaxy for NNMs.

During LVC O1 and O2, only one NNM event and corresponding host galaxy was detected. LVC O3 began on 2019 April 1 and is planned to end on 2020 April 30. Three NNMs and two NBMs (probability > 99 per cent) have been detected till the end of 2019. Though not all the electromagnetic counterparts can be confirmed, the growth of event number is very inspiring. With larger observational sample coming in the future, we can switch the study mode from case study to statistics. The observational distributions of binary compact objects and host galaxies' properties can be used to constrain all the physical models involved, helping us have a better understanding of stellar evolution, compact objects, and galaxy formation.

ACKNOWLEDGEMENTS

We acknowledge Hailiang Chen for reading our draft and providing some very useful comments and suggestions. We also would like to thank the anonymous referee for a detailed and instructive report which led to improvements in the presentation and content of our paper. JW acknowledges the support from the National Natural Science Foundation of China (NSFC) grant 11873051. FZ is supported by NSFC grants 11573062, 11973081, 11521303, the YIPACAS Foundation grant 2012048, and the Yunnan Foundation grant 2011CI053. L-XL is supported by NSFC grants 11373012, 11973014. RL is supported by NSFC grants 11773032, 118513, and the NAOC Nebula Talents Program. LG is supported by the National Key R&D Program of China (NO. 2017YFB0203300), and the Key Program of NSFC through grant 11733010. ZH is partly supported by NSFC grants 11521303, 11733008. JP acknowledges support from the National Basic Research Program of China (program 973 under grant no. 2015CB857001).

DATA AVAILABILITY

The Millennium Simulation data are available at Millennium Database (https://wwwmpa.mpa-garching.mpg.de/millennium/). The simulated kilonovae and their host galaxies catalogues produced from GABE, and data that support the figures are available from the corresponding author upon reasonable request.

REFERENCES

Abbott B. P. et al., 2017a, Phys. Rev. Lett., 119, 161101
Abbott B. P. et al., 2017b, ApJ, 848, L12
Abbott B. P. et al., 2017c, ApJ, 850, L39
Abbott B. P. et al., 2017d, ApJ, 851, L16
Abbott B. P. et al., 2019a, Phys. Rev. X, 9, 031040
Abbott B. P . et al., 2019b, ApJ, 882, L24
Adhikari S., Fishbach M., Holz D. E., Wechsler R. H., Fang Z., 2020, preprint (arXiv:2001.01025)
Anders E., Grevesse N., 1989, Geochim. Cosmochim. Acta, 53, 197
Andreoni I. et al., 2019, ApJ, 890, 131
Antier S. et al., 2020, MNRAS, 492, 3904
Arcavi I. et al., 2017, Nature, 551, 64
Argast D., Samland M., Thielemann F.-K., Qian Y.-Z., 2004, A&A, 416, 997
Arnould M., Goriely S., Takahashi K., 2007, Phys. Rep., 450, 97
Artale M. C., Mapelli M., Giacobbo N., Sabha N. B., Spera M., Santoliquido F., Bressan A., 2019, MNRAS, 487, 1675
Artale M. C., Mapelli M., Bouffanais Y., Giacobbo N., Pasquato M., Spera M., 2020, MNRAS, 491, 3419
Baiotti L., Rezzolla L., 2017, Rep. Prog. Phys., 80, 096901

Barnes J., Kasen D., 2013, ApJ, 775, 18
Bauswein A., Ardevol Pulpillo R., Janka H.-T., Goriely S., 2014, ApJ, 795, L9
Behroozi P., Wechsler R. H., Hearin A. P., Conroy C., 2019, MNRAS, 488, 3143
Belczynski K., Kalogera V., Bulik T., 2002, ApJ, 572, 407
Belczynski K., Taam R. E., Kalogera V., Rasio F. A., Bulik T., 2007, ApJ, 662, 504
Belczynski K., Repetto S., Holz D. E., O'Shaughnessy R., Bulik T., Berti E., Fryer C., Dominik M., 2016, ApJ, 819, 108
Belczynski K. et al., 2018a, preprint (arXiv:1812.10065)
Belczynski K. et al., 2018b, A&A, 615, A91
Berger E., Fong W., Chornock R., 2013, ApJ, 774, L23
Blanchard P. K. et al., 2017, ApJ, 848, L22 (Blanchard17)
Boco L., Lapi A., Goswami S., Perrotta F., Baccigalupi C., Danese L., 2019, ApJ, 881, 157
Bruzual G., Charlot S., 2003, MNRAS, 344, 1000
Burbidge E. M., Burbidge G. R., Fowler W. A., Hoyle F., 1957, Rev. Mod. Phys., 29, 547
Cameron A. G. W., 1957, PASP, 69, 201
Chabrier G., 2003, PASP, 115, 763
Chornock R. et al., 2017, ApJ, 848, L19
Chruslinska M., Belczynski K., Klencki J., Benacquista M., 2018, MNRAS, 474, 2937
Colless M. et al., 2001, MNRAS, 328, 1039
Côté B. et al., 2018, ApJ, 855, 99
Coughlin M. W. et al., 2019, ApJ, 885, L19
Coulter D. A. et al., 2017, Science, 358, 1556
Cowperthwaite P. S. et al., 2017, ApJ, 848, L17
Croton D. J. et al., 2006, MNRAS, 365, 11
D'Orazio D. J., Levin J., Murray N. W., Price L., 2016, Phys. Rev. D, 94, 023001
Dai Z. G., 2019, ApJ, 873, L13
Davis M., Efstathiou G., Frenk C. S., White S. D. M., 1985, ApJ, 292, 371
De Lucia G., Blaizot J., 2007, MNRAS, 375, 2
Dessart L., Burrows A., Ott C. D., Livne E., Yoon S.-C., Langer N., 2006, ApJ, 644, 1063
Dewi J. D. M., Podsiadlowski P., Pols O. R., 2005, MNRAS, 363, L71
Dobie D. et al., 2019, ApJ, 887, L13
Dominik M., Belczynski K., Fryer C., Holz D. E., Berti E., Bulik T., Mandel I., O'Shaughnessy R., 2012, ApJ, 759, 52
Dominik M., Belczynski K., Fryer C., Holz D. E., Berti E., Bulik T., Mandel I., O'Shaughnessy R., 2013, ApJ, 779, 72
Eggleton P. P., Fitchett M. J., Tout C. A., 1989, ApJ, 347, 998
Evans P. A. et al., 2017, Science, 358, 1565
Fernández R., Foucart F., Kasen D., Lippuner J., Desai D., Roberts L. F., 2017, Class. Gravity, 34, 154001
Fong W., Berger E., 2013, ApJ, 776, 18
Fontanot F., Springel V., Angulo R. E., Henriques B., 2012, MNRAS, 426, 2335
Gessner A., Janka H.-T., 2018, ApJ, 865, 61
Gilmore G., 2001, in Funes J. G., Corsini E. M., eds, ASP Conf. Ser. Vol. 230, Galaxy Disks and Disk Galaxies. Astron. Soc. Pac., San Francisco, p. 3
Gomez S. et al., 2019, ApJ, 884, L55
Guo Q. et al., 2011, MNRAS, 413, 101
Guo Q., White S., Angulo R. E., Henriques B., Lemson G., Boylan-Kolchin M., Thomas P., Short C., 2013, MNRAS, 428, 1351
Han Z., Podsiadlowski P., Lynas-Gray A. E., 2007, MNRAS, 380, 1098
Hansen B. M. S., Phinney E. S., 1997, MNRAS, 291, 569
Henriques B. M. B., White S. D. M., Thomas P. A., Angulo R., Guo Q., Lemson G., Springel V., Overzier R., 2015, MNRAS, 451, 2663
Hobbs G., Lorimer D. R., Lyne A. G., Kramer M., 2005, MNRAS, 360, 974
Hosseinzadeh G. et al., 2019, ApJ, 880, L4
Hurley J. R., Tout C. A., Pols O. R., 2002, MNRAS, 329, 897
Jiang L., Helly J. C., Cole S., Frenk C. S., 2014, MNRAS, 440, 2115
Jiang Z., Wang J., Gao L., Zhang F.-H., Guo Q., Wang L., Pan J., 2019, Res. Astron. Astrophys, 19, 151
Kappeler F., Beer H., Wisshak K., 1989, Rep. Prog. Phys., 52, 945
Kasen D., Badnell N. R., Barnes J., 2013, ApJ, 774, 25
Kasen D., Metzger B., Barnes J., Quataert E., Ramirez-Ruiz E., 2017, Nature, 551, 80
Kasliwal M. M. et al., 2017, Science, 358, 1559
Kauffmann G., Colberg J. M., Diaferio A., White S. D. M., 1999, MNRAS, 303, 188
Kim C., Perera B. B. P., McLaughlin M. A., 2015, MNRAS, 448, 928
Korobkin O., Rosswog S., Arcones A., Winteler C., 2012, MNRAS, 426, 1940
Lattimer J. M., Schramm D. N., 1974, ApJ, 192, L145
LIGO Scientific Collaboration et al., 2015, Class. Quantum Gravity, 32, 074001
LIGO Scientific Collaboration, VIRGO Collaboration, 2019, GRB Coordinates Network, 24168, 1
Li L.-X., 2019, ApJ, 872, 19
Li L.-X., Paczyński B., 1998, ApJ, 507, L59
Lundquist M. J. et al., 2019, ApJ, 881, L26
McMillan P. J., 2017, MNRAS, 465, 76
Madau P., Dickinson M., 2014, ARA&A, 52, 415
Maoz D., Mannucci F., Nelemans G., 2014, ARA&A, 52, 107
Mapelli M., Giacobbo N., 2018, MNRAS, 479, 4391
Mapelli M., Giacobbo N., Toffano M., Ripamonti E., Bressan A., Spera M., Branchesi M., 2018, MNRAS, 481, 5324
Mapelli M., Giacobbo N., Santoliquido F., Artale M. C., 2019, MNRAS, 487, 2
Metzger B. D., 2017, Living Revi. Relativ., 20, 3
Metzger B. D., Berger E., 2012, ApJ, 746, 48
Metzger B. D. et al., 2010, MNRAS, 406, 2650
Meyer B. S., 1994, ARA&A, 32, 153
Mingarelli C. M. F., Levin J., Lazio T. J. W., 2015, ApJ, 814, L20
Nicholl M. et al., 2017, ApJ, 848, L18
Perego A., Rosswog S., Cabezón R. M., Korobkin O., Käppeli R., Arcones A., Liebendörfer M., 2014, MNRAS, 443, 3134
Planck Collaboration XIII, 2015, A&A, 594, 63
Podsiadlowski P., Langer N., Poelarends A. J. T., Rappaport S., Heger A., Pfahl E., 2004, ApJ, 612, 1044
Portegies Zwart S. F., Yungelson L. R., 1998, A&A, 332, 173
Pozanenko A. S., Minaev P. Y., Grebenev S. A., Chelovekov I. V., 2020, Astron. Lett., 45, 710
Rosswog S., Sollerman J., Feindt U., Goobar A., Korobkin O., Wollaeger R., Fremling C., Kasliwal M. M., 2018, A&A, 615, A132
Salim S. et al., 2007, ApJS, 173, 267
Shibata M., Kyutoku K., Yamamoto T., Taniguchi K., 2009, Phys. Rev. D, 79, 044030
Smartt S. J. et al., 2017, Nature, 551, 75
Spergel D. N. et al., 2003, ApJS, 148, 175
Springel V., White S. D. M., Tormen G., Kauffmann G., 2001, MNRAS, 328, 726
Springel V. et al., 2005, Nature, 435, 629
Strolger L.-G. et al., 2004, ApJ, 613, 200
Surman R., McLaughlin G. C., Ruffert M., Janka H.-T., Hix W. R., 2008, ApJ, 679, L117
Tanaka M., Hotokezaka K., 2013, ApJ, 775, 113
Tanaka M., Hotokezaka K., Kyutoku K., Wanajo S., Kiuchi K., Sekiguchi Y., Shibata M., 2014, ApJ, 780, 31
Tanaka M. et al., 2017, PASJ, 69, 102
Tanvir N. R., Levan A. J., Fruchter A. S., Hjorth J., Hounsell R. A., Wiersema K., Tunnicliffe R. L., 2013, Nature, 500, 547
Tanvir N. R. et al., 2017, ApJ, 848, L27
Tauris T. M., Langer N., Moriya T. J., Podsiadlowski P., Yoon S. C., Blinnikov S. I., 2013, ApJ, 778, L23
Tauris T. M., Langer N., Podsiadlowski P., 2015, MNRAS, 451, 2123
Tauris T. M. et al., 2017, ApJ, 846, 170

Toffano M., Mapelli M., Giacobbo N., Artale M. C., Ghirlanda G., 2019, MNRAS, 489, 4622
Toonen S., Nelemans G., Portegies Zwart S., 2012, A&A, 546, A70
Troja E. et al., 2017, Nature, 551, 71 (Troja17)
Voss R., Tauris T. M., 2003, MNRAS, 342, 1169
Wang J., De Lucia G., Kitzbichler M. G., White S. D. M., 2008, MNRAS, 384, 1301
Wang L. et al., 2017, MNRAS, 468, 4579
Waxman E., Ofek E. O., Kushnir D., Gal-Yam A., 2018, MNRAS, 481, 3423
Wheeler J. C., Cowan J. J., Hillebrandt W., 1998, ApJ, 493, L101
White S. D. M., Frenk C. S., 1991, ApJ, 379, 52
Woosley S. E., Hoffman R. D., 1992, ApJ, 395, 202
Yu Y.-W., Liu L.-D., Dai Z.-G., 2018, ApJ, 861, 114
Yungelson L. R., 2013, in Di Stefano R., Orio M., Moe M., eds, IAU Symp. Vol. 281, Binary Paths to Type Ia Supernovae Explosions, Kluwer, Dordrecht, p. 244
Zhang B., 2019, ApJ, 873, L9
Zhang F., Han Z., Li L., Hurley J. R., 2004, A&A, 415, 117
Zhang F., Han Z., Li L., Hurley J. R., 2005, MNRAS, 357, 1088
Zhang F., Han Z., Li L., Guo J., Zhang Y., 2010, Ap&SS, 329, 249

APPENDIX A: GALAXY NUMBER DENSITY DISTRIBUTION IN GABE

Fig. A1 presents the spacial number density distribution of all galaxies at $z = 0$ in GABE, in a age–stellar mass plane. The distribution peaks at stellar mass $\sim 10^8\,M_\odot$ and age ~ 8 Gyr. Benefit from the inclusion of almost all classical galactic physical processes, GABE provides us a fair complete star formation history library for the calculation of R_{COM}. Other properties of galaxies in GABE can be found in Jiang et al. (2019).

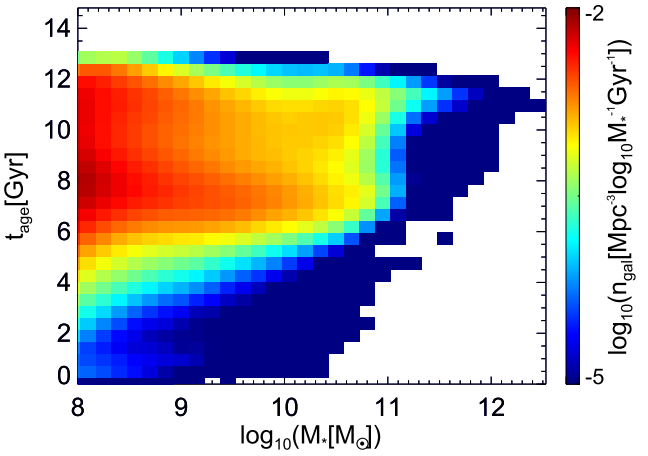

Figure A1. The number density distribution of galaxies as a function of stellar mass and mass-weighted age at $z = 0$ in GABE. Color in each cell indicates the mean number density for galaxies in the cell with values shown in the colour bar.

This paper has been typeset from a TEX/LATEX file prepared by the author.